CircURI1 interacts with hnRNPM to inhibit metastasis by modulating alternative splicing in gastric cancer

Xiaolin Wang[a,b,c,d,1] ([ORCID]), Jingxin Li[b,1], Xing Bian[a,b,c,d], Cheng Wu[e], Jinghan Hua[a,b,c,d], Shuhui Chang[b], Tianyi Yu[b], Hong Li[a,c,d], Yongxiang Li[e], Shanshan Hu[f,2], Ge Shan[b,2], and Wenchu Lin[a,c,d,2]

[a]High Magnetic Field Laboratory, Hefei Institutes of Physical Science, Chinese Academy of Sciences, Hefei 230031, China; [b]University of Science and Technology of China, Hefei 230026, China; [c]Key Laboratory of High Magnetic Field and Ion Beam Physical Biology, Hefei Institutes of Physical Science, Chinese Academy of Sciences, Hefei 230031, China; [d]High Magnetic Field Laboratory of Anhui Province, Hefei 230031, China; [e]Department of General Surgery, The First Affiliated Hospital of Anhui Medical University, Hefei 230022, China; and [f]Department of Neurosurgery, Division of Life Sciences and Medicine, University of Science and Technology of China, Hefei 230001, China

Circular RNAs (circRNAs) have emerged as key regulators of human cancers, yet their modes of action in gastric cancer (GC) remain largely unknown. Here, we identified *circURI1* back-spliced from exons 3 and 4 of unconventional prefoldin RPB5 interactor 1 (URI1) from circRNA profiling of five-paired human gastric and the corresponding nontumor adjacent specimens (paraGC). *CircURI1* exhibits the significantly higher expression in GC compared with paraGC and inhibitory effects on cell migration and invasion in vitro and GC metastasis in vivo. Mechanistically, *circURI1* directly interacts with heterogeneous nuclear ribonucleoprotein M (hnRNPM) to modulate alternative splicing of genes, involved in the process of cell migration, thus suppressing GC metastasis. Collectively, our study expands the current knowledge regarding the molecular mechanism of circRNA-mediated cancer metastasis via modulating alternative splicing.

circURI1 | gastric cancer | metastasis | hnRNPM | alternative splicing

Gastric cancer (GC) is the fifth most-common malignant tumor and the third leading cause of cancer death worldwide (1, 2). Although diverse treatment options are available, the prognosis for GC patients remains poor, largely due to the presence of metastatic spread in patients (3). Cancer metastasis is a multifactorial, multistep, and complex process influenced by environmental and genetic factors (1). The outlook for metastatic GC patients is very poor, with a median overall survival of ~8 mo (2). Understanding GC metastasis at the molecular and cellular levels will help to identify potential biomarkers for diagnosis and therapeutic targets for intervention.

Circular RNAs (circRNAs) are covalent, closed, single-stranded RNA molecules generated by back-splicing or other RNA circularization mechanisms (4–7). In contrast to linear RNAs, circRNAs lack 5′ and 3′ ends and are resistant to RNA exonuclease, providing them with promising features to serve as potential biomarkers or therapeutic targets (4). Accumulating lines of evidence have illustrated the ectopic expression patterns and fundamental regulatory functions of circRNAs in biological processes, including the cell cycle, cell growth, and metastasis (8–11). Some cytoplasmic circRNAs serve as microRNA (miRNA) sponges to lift the inhibitory effects of miRNAs on their targets (12–15). Another mechanism is that exon–intron circRNAs (EIciRNAs) promote gene expression by binding to the U1 small nuclear ribonucleoprotein complex in the nucleus (16). Furthermore, a small subset of circRNAs undergoes cap-independent translation under certain circumstances, even though the vast majority of circRNAs are thought to be noncoding (17, 18). In GC, *circPVT1* promotes cell proliferation by acting as a *miR-125b* sponge (19). As a nuclear down-regulated noncoding RNA, *circHuR* suppresses HuR expression and GC progression by inactivating CNBP (20). However, the biological functions and underlying mechanisms of circRNAs in GC progression remain largely elusive.

Alternative splicing gives rise to diverse messenger RNA (mRNA) isoforms by the different arrangements of exon organization from precursor mRNAs (pre-mRNAs), leading to encoding structurally and functionally distinct protein variants (21, 22). As a gene expression regulation event in eukaryotes, alternative splicing controlled by splicing factors such as hnRNP proteins plays fundamental roles in the progression of human cancers (23–27). For instance, PTBP1 (hnRNP I) mediates alternative splicing of *MEIS2* and *PKM* to promote lymphatic metastasis and proliferation of bladder cancer (26). Another hnRNP protein hnRNPM is known to regulate breast cancer metastasis via modulating alternative splicing of *CD44* (27); actually, the only known molecular role of hnRNPM is to modify alternative splicing (28).

To investigate the functional roles of circRNAs in GC, we performed RNA sequencing (RNA-seq) of five-paired GC and the corresponding nontumor adjacent specimens (paraGC) to identify promising circRNA candidates. We found that *circURI1* expression levels were remarkably increased in GC compared with paraGC. With a series of molecular, cellular, and biochemical experiments, we demonstrated the roles of *circURI1* in the prevention of GC metastasis and further illustrated an elegant molecular pathway, in which *circURI1* served as a decoy of hnRNPM to modulate alternative splicing of a subset of genes related to cell migration.

Results

CircRNA Profiling of GC. To systematically characterize the genome-wide landscape of circRNAs in GC, we performed

Significance

Circular RNAs (circRNAs) play increasingly appreciated gene-regulatory roles in the process of human tumorigenesis. Our results demonstrated that *circURI1* expression levels were significantly increased in gastric cancer (GC) compared to paraGC, and the depletion of *circURI1* promoted metastasis in vitro and in vivo. *CircURI1* directly interacted with hnRNPM and modulated alternative splicing by sequestering the hnRNPM protein. Our study provides a reported association of circRNA, alternative splicing, and metastasis and sheds light on the molecular mechanisms of metastatic GC.

ribosomal RNA (rRNA)–depleted RNA-seq analysis of five-paired GC and paraGC specimens to de novo identify circRNA transcripts. Principal component analysis plots revealed that the five biological replicates clustered together, while the GC and paraGC groups were clearly separated (*SI Appendix*, Fig. S1*A*). Back-spliced reads per million (BRPM) were used to evaluate circRNA expression levels. A subset of circRNAs was identified only in a fraction of 10 samples, whereas others were extensively expressed in most samples with higher expression levels (*SI Appendix*, Fig. S1 *B* and *C*). Circos plots globally displayed 4,485 and 5,008 circRNAs in GC and paraGC groups, respectively (Fig. 1*A*). Venn diagram analysis revealed the overlap of circRNAs in GC and paraGC groups, and ~60% of all 5,757 circRNA candidates were detected in both groups (*SI Appendix*, Fig. S1*D*). We further categorized the genomic distribution of circRNAs and found that more than 85% of the circRNAs consisted of protein-coding exons, whereas ~15% aligned to noncoding RNAs, intergenic regions, untranslated regions, antisense to known transcripts, and unannotated regions of the genome (*SI Appendix*, Fig. S1*E*). Simultaneously, 277 readthrough circRNAs, which are generated by exons from more than one coding gene and are relatively enriched in tumor cells (8), were annotated from our dataset (*SI Appendix*, Fig. S1*E*). Volcano plots and hierarchical cluster analysis were executed for all expressed circRNAs, in which 245 candidates were significantly dysregulated (152 downregulated and 93 up-regulated) in GC (Fig. 1*B* and *SI Appendix*, Fig. S1*F* and Table S1). Our circRNA profiling expanded the understanding of transcriptome complexity in GC.

Integrative analysis of the previously reported circRNA profiling and our RNA-seq data in GC identified two up-regulated circRNAs (*circPVT1* and *circURI1*) in all three datasets (14, 19) (Fig. 1*C*). *CircPVT1* has previously been shown to function as a *miR-125b* sponge to promote cell proliferation in GC (19); therefore, we focused on circRNA *circURI1* for further investigations.

Characterization of *circURI1* in GC. The genomic structure showed that *circURI1* (annotated as hsa_circ_0000921 in circBase), which is composed of the third and fourth exons from the human *URI1* gene, consisted of 215 nucleotides (nt) (Fig. 1*D*), flanked by two long introns containing reverse complementary *Alu* elements that promote the generation of circRNAs in either side (5, 16). Subsequently, two GC cell lines (AGS and SGC7901) were selected for further investigations due to the highest *circURI1* expression levels in five GC cell lines (*SI Appendix*, Fig. S2*A*). The putative back-spliced junction fragment of *circURI1* was validated by PCR amplification with divergent primers from complementary DNA (cDNA), but not from genomic DNA, and further confirmed by Sanger sequencing (Fig. 1*D*). Northern blot analysis confirmed the existence and full length of *circURI1* with a probe against the back-spliced junction in AGS and SGC7901 cells (Fig. 1*E*). RNase R exonuclease assay by RT-qPCR verified that *circURI1* was resistant to digestion, also demonstrating its circular nature (*SI Appendix*, Fig. S2*B*). In addition, ~115 and ~80 *circURI1* copies per cell were estimated in AGS and SGC7901 cells, respectively (*SI Appendix*, Fig. S2*C*).

Exon sequences of *URI1* between humans and mice are highly conserved (~81.1%) (*SI Appendix*, Fig. S2*D*), and we sought to examine the existence of *circURI1* derived from the same genomic region in mice. Back-spliced junction fragment of exons 3 and 4 from the murine homolog of the *URI1* gene was not detected in mouse stomach tissues (*SI Appendix*, Fig. S2*E*), and the corresponding flanking introns of the murine *URI1* gene contained no reverse complementary sequences (*SI Appendix*, Fig. S2*F*).

The function of noncoding RNA is tightly and closely associated with its subcellular location pattern (29–31); thus, we examined the cellular localization of *circURI1*. Fluorescence in situ hybridization with a probe against the back-spliced junction of

circURI1 and RT-qPCR analysis of nuclear and cytoplasmic RNAs (Fig. 1*F* and *SI Appendix*, Fig. S2 *G–I*) were conducted, demonstrating that *circURI1* was preferentially localized within the nucleus in both AGS and SGC7901 cells. Then, we examined *circURI1* expression levels in 69-paired GC and paraGC clinical samples by RT-qPCR and found that *circURI1* was pervasively and significantly up-regulated in GC compared with paraGC (Fig. 1*G* and *SI Appendix*, Fig. S3*A*). *URI1* mRNA expression levels were also significantly increased in GC compared with paraGC (*SI Appendix*, Fig. S3*B*). *CircURI1* was dramatically increased in GC compared to paraGC via fluorescence in situ hybridization (FISH) analysis of tissues (Fig. 1*H*). Simultaneously, the decreased *circURI1* expression levels were significantly associated with advanced tumor–node–metastasis stage (III through IV) tumors and metastasis in GC patients (Fig. 1*I*). All these results indicated that *circURI1* has the potential to act as a predictive biomarker or therapeutic target for GC.

CircURI1 Inhibits GC Metastasis In Vitro and In Vivo. RNA interference was applied to explore the function of *circURI1*. Targeting *circURI1* with two independent short interfering RNAs (siRNAs) against the back-spliced junction site resulted in effective knockdown of *circURI1*, whereas no detectable effects on *URI1* mRNA expression levels were observed in AGS and SGC7901 cells (Fig. 2*A* and *SI Appendix*, Fig. S4*A*). *CircURI1* knockdown with siRNAs had no significant change in the proportion of apoptotic AGS and SGC7901 cells or the cell cycle analyzed by flow cytometry (*SI Appendix*, Fig. S3 *C* and *D*). Wound-healing assays revealed that *circURI1* knockdown with either siRNA improved the migratory ability in AGS and SGC7901 cells (Fig. 2*B* and *SI Appendix*, Fig. S4*B*). Silencing of *circURI1* also enhanced the invasive ability of AGS cells via Transwell assays, as indicated by the increased number of invaded cells (Fig. 2*C*). Alternatively, antisense oligonucleotides, which target RNA for degradation via an RNase H–mediated mechanism (32–35), were applied to deplete *circURI1*, and we observed promotive effects on AGS and SGC7901 cell migration and invasion (*SI Appendix*, Fig. S4 *C–E*). Furthermore, the clustered regularly interspaced short palindromic repeats (CRISPR)/Cas9 technique was employed to generate *circURI1* knockout (KO) AGS cells, in which the complementary repeat sequences including six *Alu* elements in the fourth intron of human *URI1* were deleted, but functional intronic elements such as the splicing sites and pyrimidine tract remained unchanged (Fig. 2*D*). *URI1* mRNA expression levels were unaltered in *circURI1* KO AGS cells compared to wild-type AGS cells (Fig. 2*E*). Wound-healing and Transwell assays revealed that the migratory and invasive abilities were promoted in *circURI1* KO cells compared with wild-type (Fig. 2 *F* and *G*). In contrast, we generated a *circURI1* overexpression construct with its endogenous flanking sequences including complementary *Alu* element pairs, and *circURI1* overexpression repressed AGS cell migration and invasion (Fig. 2 *H–K*).

We established an AGS stable cell line with lentivirus short hairpin RNA to knockdown *circURI1* and confirmed the knockdown efficiency of *circURI1* (*SI Appendix*, Fig. S4*F*). We then investigated the in vivo roles of *circURI1* in metastatic potential using tail vein assay of lung metastasis. Cells with stable *circURI1* knockdown formed significantly more lung metastatic nodes and larger nodes than the control (Fig. 2*L*). These results demonstrated that *circURI1* repressed GC metastasis both in vitro and in vivo.

Interaction between *circURI1* and hnRNPM. CircRNAs have been extensively reported to function as miRNA sponges in the cytoplasm (12–15), and we doubted that *circURI1* might work as a miRNA sponge, as a portion of *circURI1* was localized in the cytoplasm (Fig. 1*F* and *SI Appendix*, Fig. S2*I*). Several putative binding miRNAs of *circURI1* (*SI Appendix*, Fig. S4*G*) were predicted with CircInteractome, a web tool for exploring the
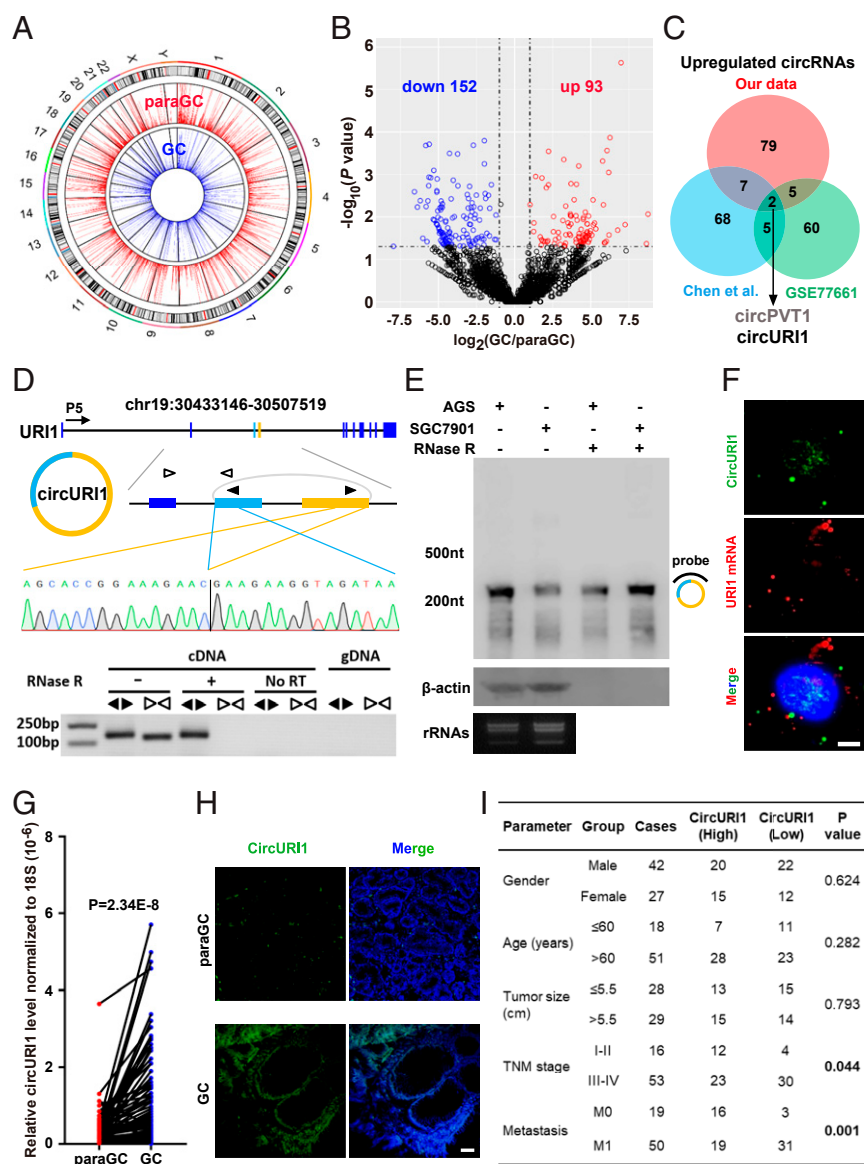
Fig. 1. Identification of *circURI1* in GC. (*A*) Circos plots showing the distribution of circRNAs in the human genome (hg19). CircRNAs with BRPM greater than 0.2 were chosen for analysis. The outer tracks represent the cytoband ideogram of the chromosome. (*B*) Volcano plots illustrating differential changes of circRNAs in GC versus paraGC samples. Blue and red dots represent significantly down-regulated and up-regulated circRNAs, respectively. (*C*) Venn diagram revealing the overlap of up-regulated circRNAs from two published datasets and our RNA-seq data in GC. Chen et al. (19) identified circRNA transcripts from three paired normal and cancerous gastric tissues, whereas GSE77661 contained RNA profiling data of one paired cancer specimen and adjacent normal tissue from a GC patient. Datasets from both Chen et al. and GSE77661 were sequenced on a 100-bp paired-end run, and our dataset was generated on a 150-bp paired-end run. (*D*) The genomic loci and validation of *circURI1*. The putative unique back-spliced junction fragment of *circURI1* (divergent primers) was performed in AGS cells by RT-PCR and validated by Sanger sequencing. P5 indicates the direction of transcription. gDNA, genomic DNA. (*E*) Northern blot analysis showing *circURI1* in AGS and SGC7901 cells. The hybridized probe against the back-spliced junction site is indicated on the right of the blot image. β-actin mRNA was the positive control for RNase R treatment. rRNA bands are presented to indicate equal loading. (*F*) RNA FISH of *circURI1* (green) with the probe antisense to the back-spliced junction indicated in the same region of Northern Blot (D) and *URI1* mRNA (red) in AGS cells. Nuclei (blue) were stained with 4, 6-diamidino-2-phenylindole. (Scale bars, 20 μm.) (*G*) RT-qPCR analysis of *circURI1* in 69-paired GC and paraGC samples. *P* value was calculated by two-tailed Student's *t* test. (*H*) RNA FISH of *circURI1* (green) in GC and paraGC tissues. (Scale bars, 1 μm.) (*I*) Relationship between *circURI1* expression and clinicopathologic factors of GC patients. *P* values were calculated by χ^2 test. Error bars indicate SEM from three independent experiments.

interaction between circRNAs and miRNAs (36). However, RNA IP (immunoprecipitation) of Ago2, the mediator of circRNA–miRNA interaction, showed significant enrichment of *circHIPK3* (as a positive control) but no detectable enrichment of *circURI1* in either AGS or SGC7901 cells (*SI Appendix*, Fig. S4H). Additionally, ribosome profiling assays confirmed no translational effect for *circURI1* in AGS cells (*SI Appendix*, Fig. S4 *I* and *J*). All these findings strongly implied that *circURI1* might function with a mechanism other than miRNA sponge and generating polypeptide.

To identify the potential protein partner of *circURI1* in GC cells, we designed a biotin-labeled DNA probe against the junction site and performed RNA pulldown assays (Fig. 3*A*). RT-qPCR indicated the effective and specific capture of *circURI1* in AGS and SGC7901 cells (Fig. 3*B*). HnRNPM, an RNA-binding protein (RBP) (37), was later determined as the *circURI1*-associated protein through mass spectrometry (MS) (Fig. 3*C* and *SI Appendix*, Fig. S5A). The interaction between *circURI1* and hnRNPM was further validated with antibodies against
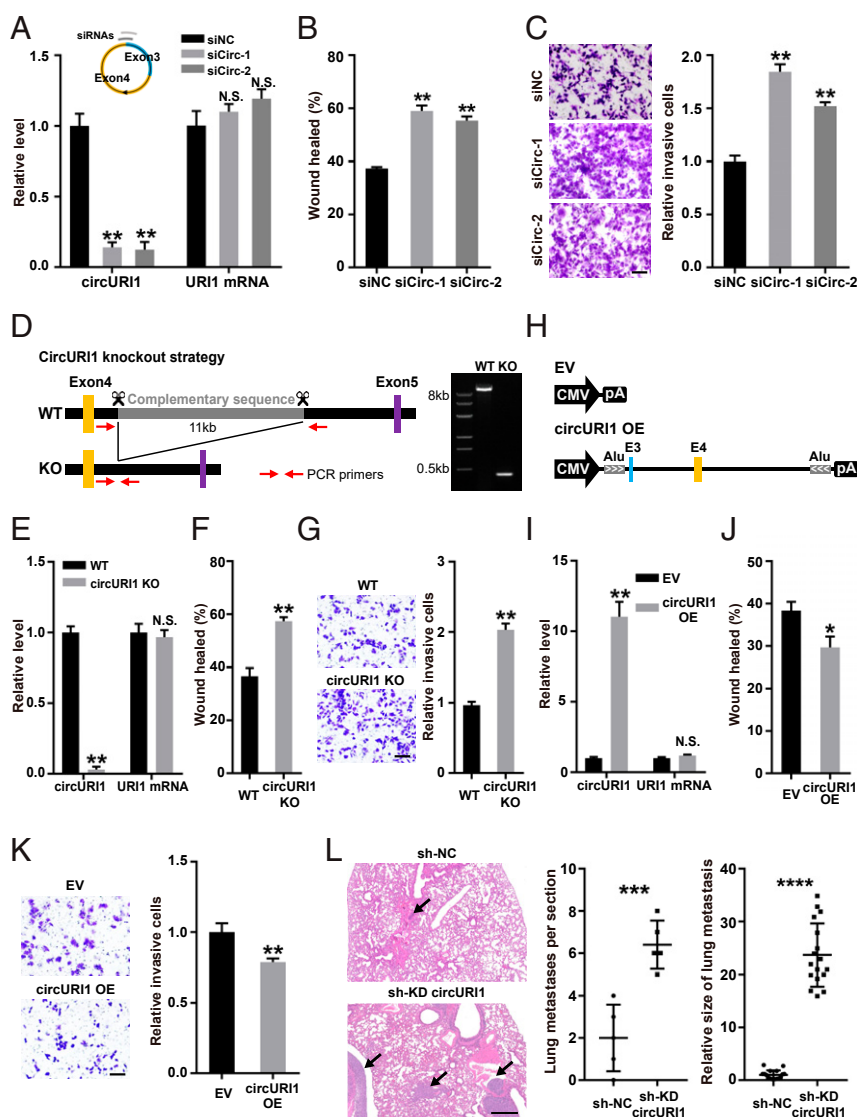
Fig. 2. *CircURI1* represses GC metastasis in vitro and in vivo. (*A*) RT-qPCR analysis of *circURI1* and *URI1* mRNA expression in AGS cells treated with two independent siRNAs against *circURI1*. siNC, siRNA with scrambled sequences; siCirc-1 and siCirc-2, two siRNAs against the junction sites of *circURI1*. (*B* and *C*) Wound-healing and Transwell assays of AGS cells treated with siRNAs targeting *circURI1*. (Scale bars, 100 μm.) (*D*) Strategy of KO reverse complementary repeats in human *URI1* intron 4 using CRISPR-Cas9 in AGS cells. Gel image of PCR products from cell genotyping is performed, and the corresponding amplifications are confirmed by Sanger sequencing. WT, wild-type; KO, deletion of the complementary repeat sequences in human *URI1* intron 4. (*E*) RT-qPCR analysis of *circURI1* and *URI1* mRNA expression in WT and *circURI1* KO AGS cells. (*F* and *G*) Wound-healing and transwell assays of WT and *circURI1* KO cells. (Scale bars, 100 μm.) (*H*) Construction of *circURI1* overexpression with its endogenous flanking sequences including the complementary *Alu* element pairs. EV, empty vector; CMV, cytomegalovirus promoter; pA, polyadenylation signal. (*I*) RT-qPCR analysis of *circURI1* and *URI1* mRNA expression upon *circURI1* overexpression. EV, empty vector. (*J* and *K*) Wound-healing and Transwell assays of AGS cells after *circURI1* overexpression. EV, empty vector. (Scale bars, 100 μm.) (*L*) Severe combined immunodeficient mice were administered an intravenous injection of the AGS stable cell line with *circURI1* knockdown and the control (*n* = 5 per group), and sectioning of the lung followed by H&E staining was performed to visualize lung metastasis. Black arrows indicate the metastatic tumor. sh-KD *circURI1*, stable cell line with lentivirus shRNA to knockdown *circURI1*; sh-NC, negative control cells for knockdown *circURI1*. Error bars indicate SEM from three independent experiments. N.S., not significant; *$P < 0.05$; **$P < 0.01$; ***$P < 0.001$; ****$P < 0.0001$ by two-tailed Student's *t* test.

endogenous hnRNPM to examine the RNAs coimmunoprecipitated with hnRNPM (RNA IP) in AGS and SGC7901 cells (Fig. 3*D*). To further characterize the interaction between *circURI1* and hnRNPM, we examined the sedimentation patterns of whole-cell materials from AGS cells with a 5 to 30% sucrose gradient. Briefly, total-cell lysate was loaded on sucrose gradients, and the corresponding gradients were divided into 12 fractions for later analysis after ultracentrifugation. The hnRNPM protein was mainly present in fractions 4 through 6, whereas the *circURI1* levels examined by RT-qPCR were also enriched in fractions 4 through 6, with some presence in fractions 10 through 12 (Fig. 3*E*).

The hnRNPM protein consists of three RNA recognition motifs (RRMs) tandemly split across the structure (Fig. 4*A*). To depict the domain required for the interaction, full-length and a variety of truncated forms of hnRNPM were overexpressed in AGS cells. RNA IP for hnRNPM and its truncations illustrated that the RRM1 domain (71 through 149 amino acids) was responsible for the interaction with *circURI1* (Fig. 4 *B* and *C*). Individual–nucleotide resolution crosslink immunoprecipitation (iCLIP) followed with RNA-seq is a powerful method to directly identify the cross-linked nucleotides of RNA bound to an RBP of interest (38-41). iCLIP-seq of FLAG-tagged hnRNPM was
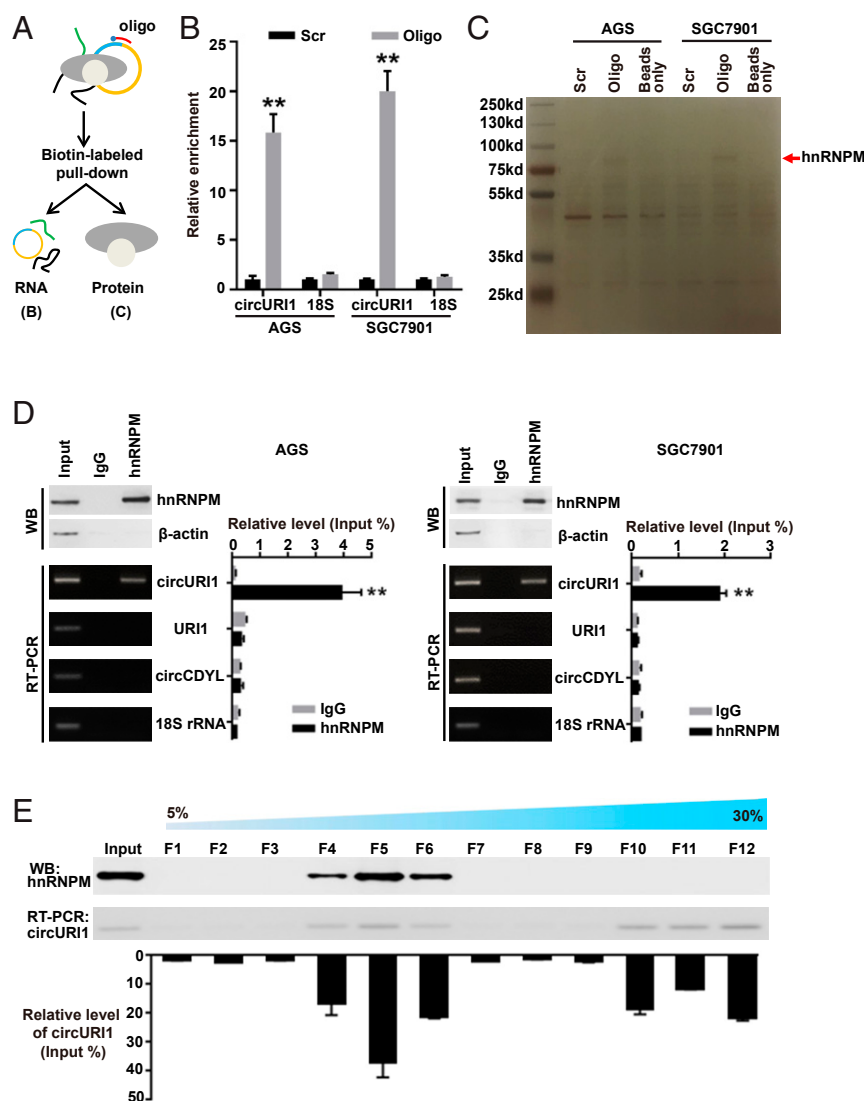
Fig. 3. The interaction between *circURI1* and hnRNPM in GC cells. (*A*) Illustration of the experimental procedure for the *circURI1* pulldown assay with biotinylated antisense oligonucleotides. (*B*) Pulldown efficiency of *circURI1* in AGS and SGC7901 cells. 18S rRNA was a negative control. Scr, biotin-labeled oligonucleotide with scrambled sequences; Oligo, biotin-labeled oligonucleotide with antisense sequences to the back-spliced junction site. (*C*) Potential *circURI1*-associated proteins identified via SDS-PAGE followed by silver staining. The red arrow denotes the band identified as hnRNPM by MS. (*D*) The specific association of hnRNPM and *circURI1* demonstrated by Western blot and RT-PCR, respectively, based on hnRNPM RNA IP in AGS and SGC7901 cells. β-actin was a negative control for Western blot (WB), and *URI1* mRNA, *circCDYL*, and *18S* rRNA were used as negative controls for RT-PCR. (*E*) Sedimentation patterns of endogenous hnRNPM and *circURI1* in 5 to 30% sucrose gradients from AGS whole-cell lysates. The components from the fractions of the gradients were determined by Western blot analysis for hnRNPM and RT-PCR for *circURI1*. Error bars indicate SEM from three independent experiments. **$P < 0.01$ by two-tailed Student's *t* test.

then performed in AGS cells, and a total of 314 hnRNPM binding targets were identified (Fig. 4*D* and *SI Appendix*, Table S2). The binding motif of hnRNPM was deduced from iCLIP-seq in AGS cells (Fig. 4*E*), which was inconsistent with the reported GU-rich motif often containing a UU sequence of hnRNPM–RNA interactions in 293T cells (42). HnRNPM iCLIP-seq determined that a 19-nt sequence (GGCUGUAGGUUUAGUUGAG), which was proximal to the junction site of *circURI1*, was the hnRNPM binding site (Fig. 4*F*). We also investigated the hnRNPM–*circURI1* interaction with a method we termed individual-CLIP, which could be used to identify the binding site of a RBP on individual RNA target of interest (*SI Appendix*, Fig. S5*B*). The same 19-nt binding site in *circURI1* was identified via hnRNPM individual-CLIP (*SI Appendix*, Fig. S5*C* and Table S3). Consistently, mutation of the 19-nt binding site in *circURI1* (*circURI1-M19*) abolished the interaction between hnRNPM

and *circURI1* (Fig. 4*G* and *SI Appendix*, Fig. S5 *D* and *E*). *CircURI1* but not *circURI1-M19* could rescue the promotive effect of *circURI1* KO on AGS cell migration and invasion (Fig. 5 *A–C*). Our results demonstrated that hnRNPM with its RRM1 domain interacted with *circURI1* through the 19-nt RNA sequence.

Effects of *circURI1* and hnRNPM on Cell Migration and Invasion in GC. HnRNPM was recently proposed to modulate RNA alternative splicing in association with cancer metastasis (43, 44). Roles of hnRNPM in GC remain largely unknown. Box plots analyzed from The Cancer Genome Atlas (TCGA) datasets showed extremely higher *hnRNPM* expression levels in GC compared with normal tissues (*SI Appendix*, Fig. S6*A*). Knockdown of either *circURI1* or *hnRNPM* did not change the expression level of the other interaction partner; hence, suggesting that these partners do
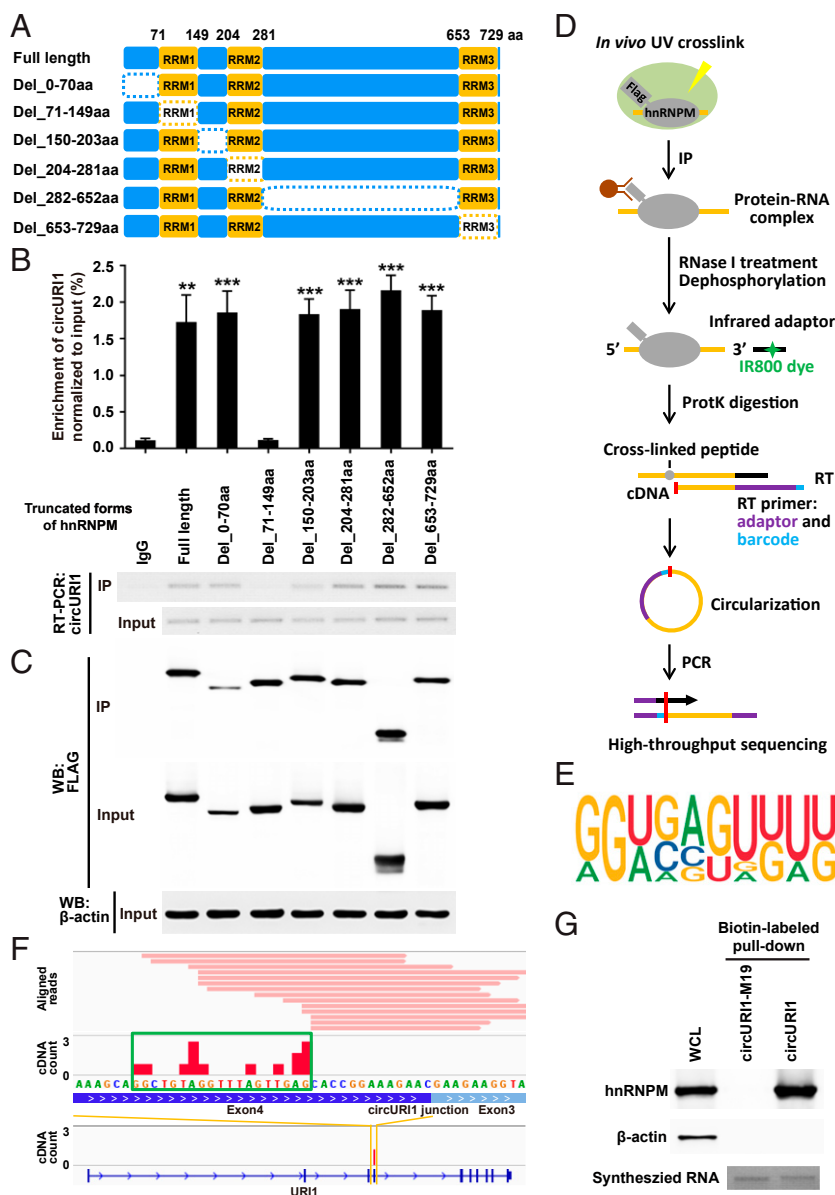
Fig. 4. The RRM1 domain of hnRNPM and the 19-nt sequence of *circURI1* are required for their interaction. (*A*) Schematic diagram revealing full-length hnRNPM and a variety of truncated forms of hnRNPM. The dotted rectangles indicate the truncated domains. (*B* and *C*) Association of *circURI1* examined by RT-PCR and RT-qPCR with RNA IP of Flag-tagged full-length and truncated hnRNPM in AGS cells. Full-length and truncated forms of hnRNPM were determined by Western blot with an anti-FLAG antibody. β-actin was a loading control for Western blot. (*D*) Illustration of the experimental procedure of iCLIP-seq. (*E*) The binding motif of hnRNPM derived from iCLIP analyzed by Hypergeometric Optimization of Motif EnRichment (HOMER). (*F*) Individual Flag-hnRNPM iCLIP-seq reads (in pink) were aligned to *circURI1* or *URI1* mRNA. iCLIP-seq cDNA counts (in red) showing the binding signals. The binding site of hnRNPM on *circURI1* deduced from iCLIP-seq is depicted with the green rectangle. (*G*) RNA pulldown assay of biotin-labeled *circURI1* and *circURI1* with the mutation of the 19-nt binding site (*circURI1-M19*) followed by Western blot with an anti-hnRNPM antibody. *CircURI1* and *circURI1-M19* were circularized in vitro. Agarose gel performed in vitro synthesized biotin-labeled *circURI1* and *circURI1-M19*. β-actin was a negative control for Western blot. WCL, whole-cell lysis. Error bars indicate SEM from three independent experiments. **$P < 0.01$; ***$P < 0.001$ by two-tailed Student's *t* test.

not transcriptionally regulate or destabilize each other (Fig. 5 *D* and *E* and *SI Appendix*, Fig. S6 *B* and *C*). Knockdown of *hnRNPM* with two independent siRNAs obviously reduced cell migration in AGS and SGC7901 cells (*SI Appendix*, Fig. S6*D*). We also found that depletion of *hnRNPM* significantly diminished AGS cell invasion (*SI Appendix*, Fig. S6*E*), consistent with previous observations in breast cancer (27). These results provided evidence that depletion of *hnRNPM* impaired cell migration and invasion, which yielded the opposite effects of *circURI1* inhibition.

Then, knockdown of *hnRNPM* recovered the migratory ability of AGS and SGC7901 cells with *circURI1* knockdown (*SI*

Appendix, Fig. S6 *F* and *G*). Similarly, silencing *hnRNPM* also rescued the invasion-promoting effect of *circURI1* knockdown on AGS cell invasion (*SI Appendix*, Fig. S6*H*). *CircURI1* but not *circURI1-M19* blocked the promoting effect of hnRNPM overexpression on AGS cell migration and invasion (Fig. 5 *F* and *G*). Additionally, full-length hnRNPM (FL) but not hnRNPM without the RRM1 domain (Del_71 through 149aa) reversed the repressive effect of *circURI1* overexpression on AGS cell migration and invasion (Fig. 5 *H* and *I*). HnRNPM (FL) exhibited a more promotive effect on cell invasion than hnRNPM (Del_71 through 149aa) in *circURI1* KO AGS cells, indicating that the
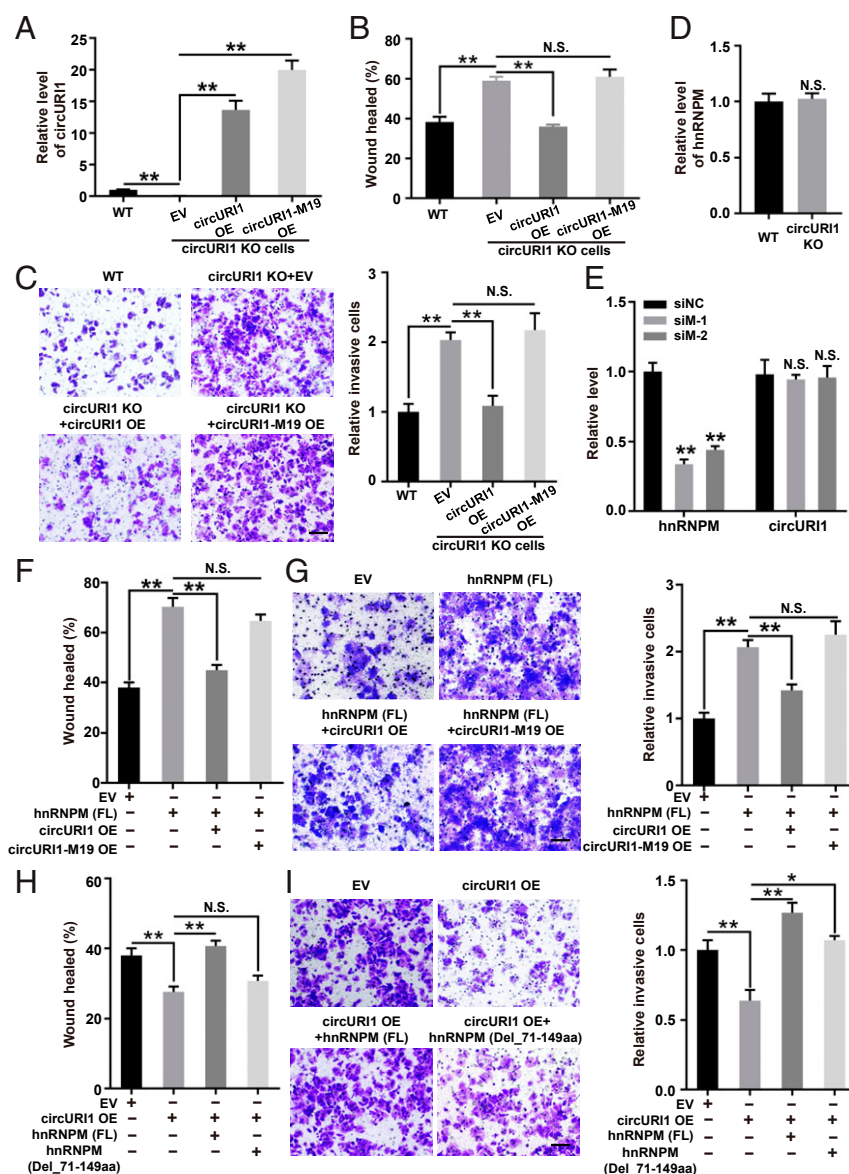
Fig. 5. The effects of *circURI1* and hnRNPM on GC cell migration and invasion. (*A*) RT-qPCR analysis of *circURI1* expression levels in WT or *circURI1* KO AGS cells with ectopic *circURI1* overexpression (OE) and *circURI1* with the 19-nt mutation (*circURI1-M19*). (*B* and *C*) Wound-healing and Transwell assays in WT or *circURI1* KO AGS cells with overexpressing *circURI1* or *circURI1-M19*. (Scale bars, 100 μm.) (*D*) RT-qPCR analysis of *hnRNPM* expression levels in WT and *circURI1* KO cells. (*E*) RT-qPCR analysis of knockdown efficiency of *hnRNPM* and *circURI1* expression levels in AGS cells treated with two siRNAs against hnRNPM. siNC, siRNA with scrambled sequences; siM-1 and siM-2, two independent siRNAs against hnRNPM. (*F* and *G*) Wound-healing and Transwell assays of AGS cells transfected with full-length hnRNPM (hnRNPM [FL]) or co-overexpressed with *circURI1* and *circURI1-M19*. (Scale bars, 100 μm.) (*H* and *I*) Wound-healing and Transwell assays of AGS cells overexpressing *circURI1* or co-overexpressing hnRNPM truncated forms including hnRNPM (FL) and hnRNPM without the RRM1 domain (hnRNPM [Del_71-149aa]). (Scale bars, 100 μm.) Error bars indicate SEM from three independent experiments. N.S., not significant; *$P < 0.05$; **$P < 0.01$ by two-tailed Student's *t* test.

circURI1-interacting domain RRM1 is required for the observed cellular phenotypes (*SI Appendix*, Fig. S6*I*). Taking these results together, we concluded that roles of *circURI1* on cell migration and invasion were dependent on its interaction with hnRNPM.

CircURI1 Modulates Alternative Splicing via Sequestering hnRNPM. To provide insight into the mechanism of *circURI1* and hnRNPM in GC, we silenced the expression levels of *hnRNPM* and *circURI1* in AGS cells and performed RNA sequencing. HnRNPM knockdown resulted in 231 alternative splicing exons (termed hnRNPM-sensitive exons) with marked alterations in AGS cells (Fig. 6*A* and *SI Appendix*, Table S4), in line with previous findings

about hnRNPM in exon inclusion or exclusion in 293T cells (44). HnRNPM iCLIP-seq showed more bindings in the flanking introns of the hnRNPM-sensitive exons than those of the insensitive exons (*SI Appendix*, Fig. S7*A*). Gene Ontology analysis for parental genes of 231 hnRNPM-sensitive exons demonstrated a biological process associated with endothelial cell migration (*SI Appendix*, Fig. S7*B*). *CircURI1* knockdown led to 29 alternative splicing exons (termed *circURI1*-sensitive exons) with significant dysregulation (Fig. 6*A* and *SI Appendix*, Table S4). Venn diagram showed that the 22 exons were both sensitive to *circURI1* and hnRNPM (Fig. 6*A*). The observed changes in both *circURI1* and hnRNPM-sensitive exons exhibited a negative correlation (Fig. 6*B*).

CELL BIOLOGY

CHEMISTRY

Gene Ontology analysis for parental genes of both *circURI1-* and hnRNPM-sensitive exons illustrated biological processes associated with cell migration, endothelial cell chemotaxis, cellular response to hypoxia, peptidyl-Ser phosphorylation, and epithelial cell proliferation (Fig. 6C). Experimental validations with semi-quantitative RT-PCR were conducted to examine the changes in alternative splicing for 10 genes (five exon inclusions and five exon exclusions) upon knockdown of *circURI1* or *hnRNPM* (Fig. 6D and *SI Appendix*, Fig. S7C). The results confirmed that *circURI1* could induce specific exon inclusion and exclusion. More importantly, it was clear that *circURI1* influenced inclusion or exclusion in contrast to hnRNPM (Fig. 6D and *SI Appendix*, Fig. S7C). De novo motif analysis of flanking introns for the 22 *circURI1-* and hnRNPM-sensitive exons showed that the most-enriched motif was a UUGUUU sequence, similar to the 19-nt sequences in *circURI1*

identified by hnRNPM iCLIP-seq (Fig. 7A), which was distinct from the motifs of flanking introns for 209 *circURI1* insensitive and hnRNPM-sensitive exons (*SI Appendix*, Fig. S7D). After *circURI1* knockdown in AGS cells, hnRNPM binding to pre-mRNA of *circURI1*-sensitive genes was significantly increased (Fig. 7 B–D). In addition, 22 *circURI1*-sensitive exons are relative more sensitive to hnRNPM knockdown (*SI Appendix*, Fig. S7E). All these results indicated that *circURI1* served as a decoy of hnRNPM to modulate alternative splicing.

Alternative Splicing of VEGFA Is a Functional Target of *circURI1*. To further elucidate the clinical relevance of alternative splicing mediated by *circURI1* and hnRNPM, we evaluated the association between the changes in alternative splicing of the four genes (*VEGFA*, *LGALS8*, *AKT1*, and *NR4A1*) involved in the process
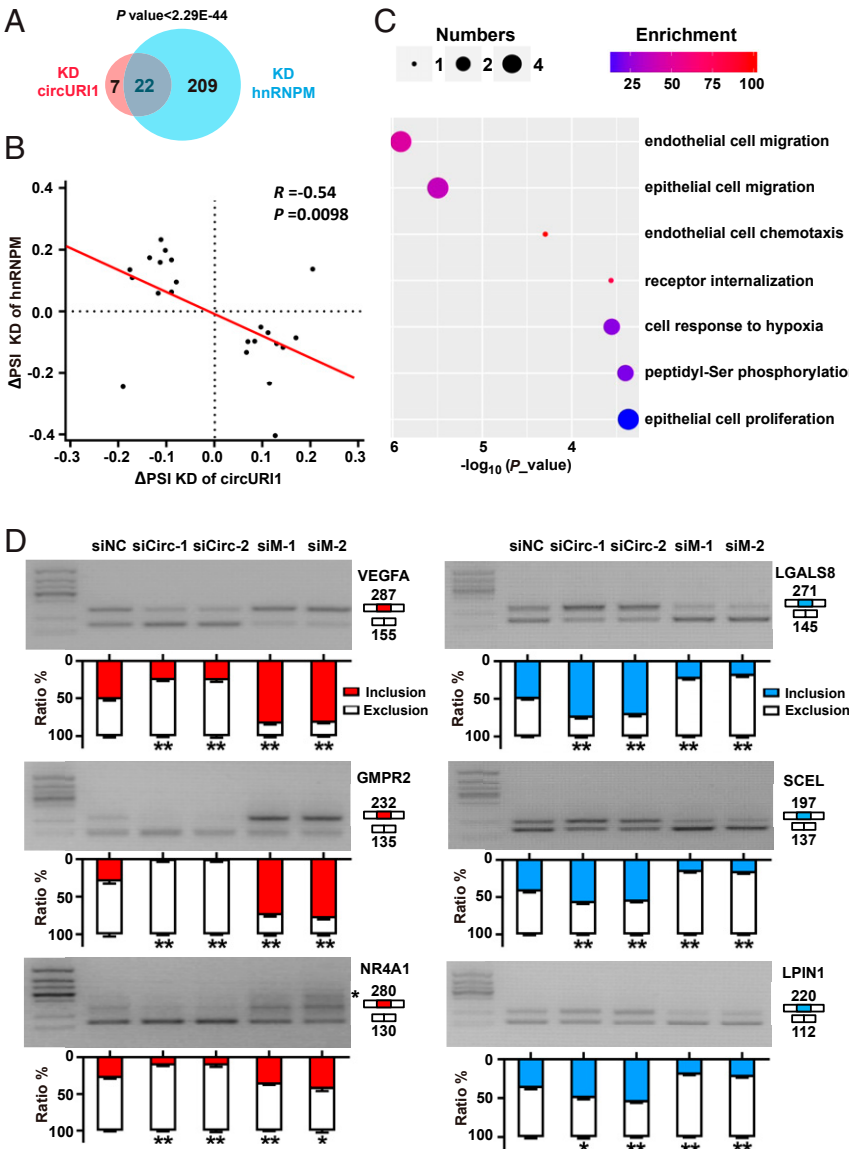

Fig. 6. The effects of *circURI1* and hnRNPM on alternative splicing. (*A*) Venn diagram illustrating the overlap of altered alternative splicing events upon depleting *circURI1* or *hnRNPM* in AGS cells. *P* value was calculated by χ^2 test. (*B*) Correlation plot of ΔPSI for exons sensitive to both *circURI1* and hnRNPM. The PSI was used to calculate the changes in alternative splicing. R represents Spearman's correlation coefficient, and the *P* value was calculated by Spearman's correlation test. (*C*) Gene Ontology analysis of both *circURI1* and hnRNPM-sensitive exons analyzed by Gorilla. (*D*) Semi-quantitative RT-PCR validation of both *circURI1* and hnRNPM-sensitive exons upon knockdown of *circURI1* or *hnRNPM* in AGS cells. For *NR4A1*, an unspecific band is also amplified (indicated with a star). siNC, siRNA with scrambled sequences; siCirc-1 and siCirc-2, two siRNAs against the junction sites of *circURI1*; siM-1 and siM-2, two independent siRNAs against hnRNPM. Error bars indicate SEM from three independent experiments. *$P < 0.05$; **$P < 0.01$ by two-tailed Student's *t* test.
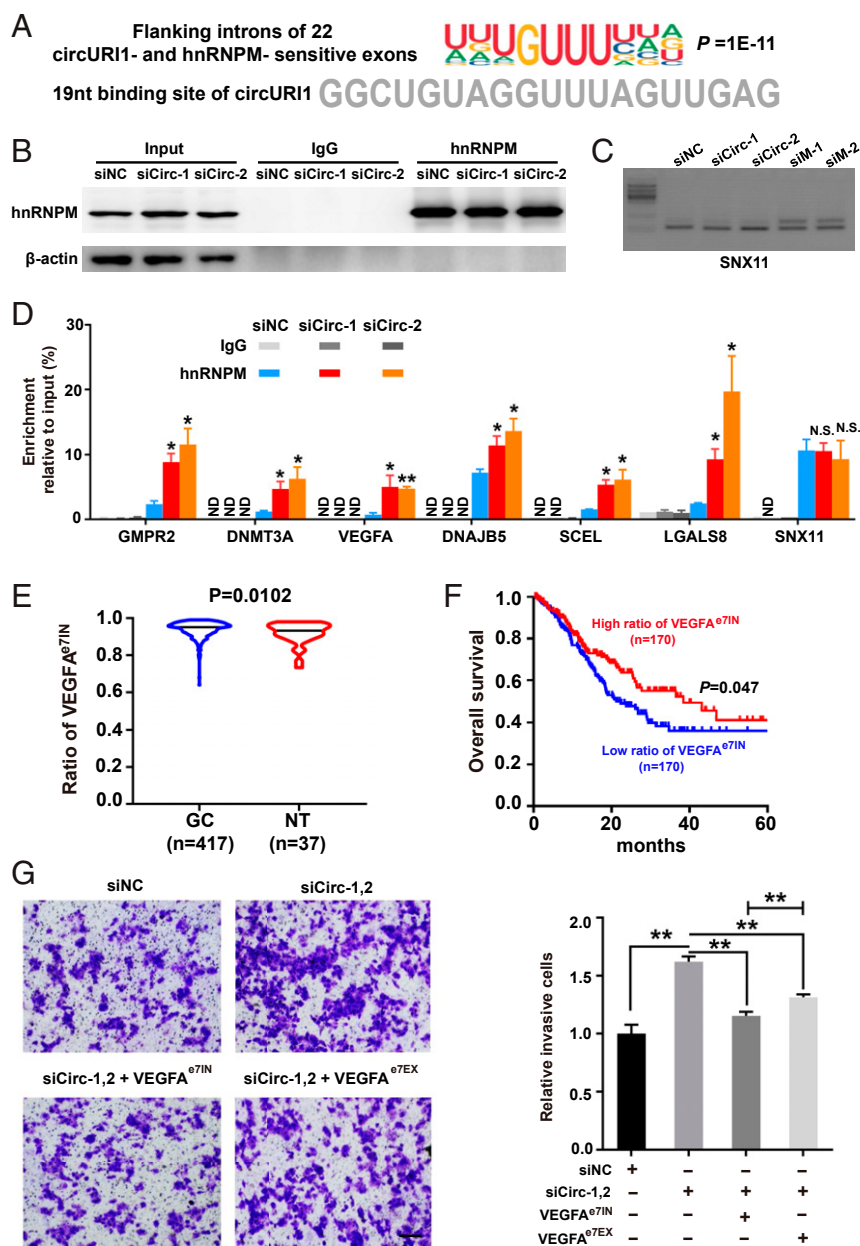
Fig. 7. *CircURI1* modulates alternative splicing via sequestering hnRNPM. (*A*) The deduced motif of introns flanked by 22 both *circURI1* and hnRNPM-sensitive exons analyzed by HOMER (-len 10). The 19-nt sequence of *circURI1* required for the interaction of hnRNPM is indicated below. (*B*) RNA IP efficiency of hnRNPM demonstrated by Western blot after *circURI1* silencing in AGS cells. β-actin was a negative control for RNA IP. siNC, siRNA with scrambled sequences; siCirc-1 and siCirc-2, two siRNAs against the junction sites of *circURI1*. (*C*) Semi-quantitative RT-PCR validation of alternatively spliced exon in sorting nexin 11 (SNX11), a hnRNPM-sensitive gene not sensitive to *circURI1*, upon silencing *circURI1* or hnRNPM in AGS cells. siM-1 and siM-2, two independent siRNAs against hnRNPM. (*D*) RNA IP of hnRNPM showing the binding for the corresponding pre-mRNAs of *circURI1*-sensitive targets upon *circURI1* knockdown in AGS cells. SNX11 was a negative control. ND, no detection. (*E*) Violin plots depicting the ratio of $VEGFA^{e7IN}$ in GC and normal patients analyzed from TCGA database. NT, normal tissue. $VEGFA^{e7IN}$, exon 7 inclusion of *VEGFA*. (*F*) Kaplan–Meier analysis of overall survival for GC patients with $VEGFA^{e7IN}$ from TCGA database. The red curve represents survival in GC patients with a high ratio of $VEGFA^{e7IN}$, and the blue line represents survival in patients with a low ratio of $VEGFA^{e7IN}$. (*G*) Transwell assays of AGS cells treated with siRNAs targeting *circURI1* or co-overexpressing $VEGFA^{e7IN}$ or $VEGFA^{e7EX}$. siNC, siRNA with scrambled sequences; siCirc-1,2, two siRNAs (siCirc-1, siCirc-2) against the junction sites of *circURI1*. (Scale bars, 100 μm.) Error bars indicate SEM from three independent experiments. In *D*, *E*, and *G*, N.S., not significant; *$P < 0.05$; **$P < 0.01$ by two-tailed Student's *t* test. In *F*, *P* value by the log-rank test.

of cell migration and clinicopathological features of GC. Our results demonstrated that *circURI1* could promote exon 7 inclusion of *VEGFA* ($VEGFA^{e7IN}$), exon 8 exclusion of *LGALS8* ($LGALS8^{e8EX}$), exon 2 inclusion of *AKT1* (AKT^{e2IN}), and exon 2 inclusion of *NR4A1* ($NR4A1^{e2IN}$) (Fig. 6 and *SI Appendix*, Table S4). Violin analysis of TCGA database concertized that the

ratios of $VEGFA^{e7IN}$ and $LGALS8^{e8EX}$ were significantly higher in GC compared with normal tissues, while AKT^{e2IN} and $NR4A1^{e2IN}$ had no significances between GC and normal tissues (Fig. 7*E* and *SI Appendix*, Fig. S7F). Furthermore, Kaplan–Meier survival curve analysis of TCGA database revealed that the overall survival of GC patients with a high ratio of $VEGFA^{e7IN}$

Wang et al.
CircURI1 interacts with hnRNPM to inhibit metastasis by modulating alternative splicing in
gastric cancer

PNAS | 9 of 12
https://doi.org/10.1073/pnas.2012881118

was obviously longer compared with that of GC patients with a low ratio of *VEGFA*[e7IN] (Fig. 7F). Meanwhile, *LGALS8*[e8EX], *AKT*[e2IN], and *NR4A1*[e2IN] had no significant correlation to the survival of GC patients (*SI Appendix*, Fig. S7G). Finally, VEG-FA[e7IN] isoform possessed a greater ability to recover the pro-motive effect of *circURI1* knockdown on AGS cell invasion than *VEGFA*[e7EX] (Fig. 7G). We concluded that alternative splicing of *VEGFA* is a functional target of *circURI1*.

Discussion

Here, we uncovered that *circURI1*, a predominantly nuclear circRNA, had significantly higher expression levels in GC versus paraGC tissues and repressive effects on GC metastasis in vitro and in vivo, indicating that *circURI1* exerted a potent anti-metastatic activity. Mechanistically, *circURI1* exhibited its pro-tecting roles in cancer metastasis via sequestering hnRNPM protein to modulate alternative splicing in a subset of metastasis-related genes such as *VEGFA*. The identification of a circRNA playing anti-metastasis roles through modulating alternative splicing as a protein decoy is a breakthrough in cancer research.

Many circRNAs, such as *CDR1as* and *circBoule*, are conserved across species (45–47). Our results demonstrated that circulari-zation of human *circURI1* was facilitated through the flanking reverse complementary *Alu* elements (Fig. 2 *D* and *H*) and not regulated by hnRNPM (Fig. 5 *D* and *E*), which was recently reported to control circRNA biogenesis (48). However, we could not exclude the possibility that other RBPs might be responsible for the generation of *circURI1*. *CircURI1* is not detected in mice, which may be due to the lack of reverse complementary se-quences in the corresponding flanking introns of the murine *URI1* gene (*SI Appendix*, Fig. S2 *E* and *F*), demonstrating that *circURI1* is not evolutionarily conserved.

CircURI1 expression level is increased in GC compared to paraGC, although it seems that this molecule with repressive roles needs to be down-regulated for the metastasis. Two long noncoding RNAs (lncRNAs), TFPI2AS1 and LINC00460, be-have like *circURI1* in other cancer types (49, 50). TFPI2AS1 is markedly up-regulated in non–small-cell lung cancer and sup-presses cell proliferation and migration (49), and LINC00460 is significantly up-regulated in colorectal cancer (CRC) and yet exhibits inhibitory effects on CRC proliferation (50). Coding genes such as ERK3 have been shown to be transcriptionally up-regulated in non-melanoma skin cancers, and higher ERK3 ex-pression also suppresses cell migration (51, 52). In addition to the up-regulation in GC, *circURI1* was also detected in diverse 30 samples including cancer cells and multiple tissues employed in circBase database, indicating its importance beyond GC.

Considering that URI1 functions as an oncogene in ovarian cancer cells (53), our series of results excluded the *cis* roles of *circURI1* on *URI1* mRNA in GC cells. Sucrose density gradient centrifugation showed two potential *circURI1*-associated com-plexes in AGS cells. Consistent with this result, *circURI1* was localized in both the nucleus and cytoplasm in GC cells (Fig. 1F). The light complex was consistent with hnRNPM and very likely localized within the nucleus and probably required for modu-lating alternative splicing of genes involved in the process of cell migration. It is appealing to suspect that the *circURI1*-associated high molecular weight complex might also play essential roles in GC as well. Understanding the molecular and cellular roles of the *circURI1*-associated high molecular weight complex and cy-toplasmic *circURI1* would further extend our knowledge about the functions of *circURI1* in the pathogenesis of GC.

We identified 29 alternative splicing exons as the core of *cir-cURI1* targets through RNA-seq and overlapped with the targets of hnRNPM to obtain 22 exons sensitive to both *circURI1* and hnRNPM. The parental genes for the 22 exons were enriched for several functions, including endothelial cell migration and epi-thelial cell migration. It is well known that angiogenesis is an

important initial step in cancer metastasis (54). Alternative splicing of *VEGFA*, which plays key roles in vascular development in the four genes involved in the process of cell migration, is sig-nificantly associated with patient survival (Fig. 7F). The VEGF-signaling pathway is a clinically validated therapeutic target for several pathological cancers, and targeting VEGFR-2 with the antibody ramucirumab proved useful in second-line treatment of advanced GC (55–57). Given that VEGFA is frequently amplified in the chromosome instability subtype of GC (58) and *VEGFA*[e7IN] is promoted by *circURI1*, it would be interesting to assess whether higher *circURI1* expression copes with the increased requirement of alternative splicing of VEGFA during the progression of GC and has an effect on clinical outcomes of patients receiving ramucirumab. We could not rule out the probability that other targets in addition to *VEGFA*, such as *LGALS8* and *AKT1*, to-gether contribute to GC metastasis of the *circURI1*/hnRNPM axis.

Noncoding RNAs play crucial roles in the regulation of al-ternative splicing with several mechanisms (59, 60). For instance, lncRNA NEAT1 regulates the phosphorylation status of splicing factors to affect alternative splicing (59). LncRNA 5S-OT coordi-nates with U2AF65 to regulate alternative splicing via RNA:RNA pairing (60). In the present study, we demonstrated that *circURI1* sequestered hnRNPM protein to modulate alternative splicing to repress GC metastasis. Similarly, a recent investigation revealed that *circHomer1a* regulated alternative splicing of disease-associated genes with an unknown mechanism (61). Based on our data, we suspected that the binding affinity of *circURI1* and hnRNPM was greater than that of *circURI1*-sensitive exons' flanking introns and hnRNPM, leading to the competition of *circURI1* to hnRNPM to modulate alternative splicing.

In conclusion, we performed circRNA profiling and identified *circURI1* as a significantly up-regulated circRNA in GC compared with paraGC. *CircURI1* inhibited GC metastasis by sequestering hnRNPM protein to modulate alternative splicing of a small subset of genes involved in cell motility, intimating a potential self-preservation mechanism against tumor metastasis. To our knowledge, *circURI1* is the only circRNA to manipulate alternative splicing involved in cancer metastasis, expanding the vital roles of circRNAs in human health.

Methods

CircRNA Identification. For circRNA prediction, we identified the circRNA candidates with find_circ (13), and the junction reads were calculated as BRPM. In brief, the adapters were first trimmed with cutadapt to obtain clean reads, and the left reads were then aligned to the human genome (hg19) with bowtie2 allowing one mismatch. The reads continuously aligned to the reference genome were filtered out, and the remaining reads were subjected to following analysis. The 20-mers from both ends were extracted and aligned independently to find unique anchor positions. Finally, we ex-tended the anchor alignments to detect the breakpoints flanked by GU/AG splice sites. The differentially expressed circRNAs with the genomic length ≤100kb (*SI Appendix*, Table S1) were determined by DESeq2 with the criterion of $P \leq 0.05$, BRPM ≥ 0.2, and |log2(fold change)| ≥ 1.

Analysis of Alternative Splicing. Alternative splicing analysis was performed with the previously described pipeline (60), and the percentage spliced in (PSI) denotes the fraction of mRNAs that represent the inclusion isoform. Briefly, the continuous reads aligned to the human genome (hg19) were filtered out with Bowtie, allowing two mismatches. The left unmapped reads were aligned to a custom library of exon–exon junctions (EEJs) with Bowtie (version 2-m 20-best) with at least a 4-nt overhang. The custom EEJ library was generated by using existing RNA-seq data, expressed sequence tag and cDNA evidence, gene annotations, and evolutionary conservation. For the case of single-exon kipping events, we generated EEJs for E1AS, ASE2, and E1E2 (AS represents the alternative exon, and E1 and E2 represent the neighboring constitutive exons).

$$PSI = [\Sigma(E1AS) + \Sigma(ASE2)]/[\Sigma(E1AS) + 2\Sigma(E1E2) + \Sigma(ASE2)]$$

ΔPSI was calculated by subtracting the PSI of the knockdown group from that of the control, and *P* values were generated with χ^2 test. The

dysregulated alternative splicing (*SI Appendix*, Table S4) was determined with the criterion of $P \leq 0.05$ and $|\Delta PSI| \geq 0.05$.

Northern Blotting. Northern blotting was carried out as previously described (62). For probe preparation, antisense digoxigenin-labeled RNA probes were synthesized with a DIG Northern Starter Kit (Roche) according to the manufacturer's protocol. The corresponding PCR fragments were used as templates for T7 transcription in vitro. The primers for the amplification of the antisense probe were listed in *SI Appendix*, Table S5.

Ribosome Profiling. Ribosome profile analysis was carried out as previously described (63). A total of 10^7 cells were treated with ice-cold phosphate-buffered saline or culture medium containing 100 mg/mL cycloheximide (Sigma) for 10 min followed by lysis in ribosome lysis buffer (10 mM Tris·HCl [pH 7.4], 5 mM $MgCl_2$, 100 mM KCl, 1% Triton X-100, 3 mM dithiothreitol [DTT], 100 mg/mL cycloheximide, 5 U/mL RNase inhibitor [Promega], and 1× Protease-inhibitor mixture [Roche]). Polysomes were separated on a 20 to 50% linear sucrose gradient containing 20 mM Tris (pH 7.4), 5 mM $MgCl_2$, 100 mM KCl, 3 mM DTT, 100 mg/mL cycloheximide, and 1 U/mL RNase inhibitor (Promega) and centrifuged at 38,000 rpm for 4 h in a Beckman SW41 Ti rotor. The gradients were fractionated with optical scanning at 254 nm using a Gradient Fractionator (BioComp).

In Vivo Tumor Metastasis Assay. The animal studies were approved by the Institutional Animal Care and Use Committee of Hefei Institutes of Physical Science, Chinese Academy of Sciences. BABL/c 6-wk-old male nude mice were maintained under specific pathogen-free conditions, with individually ventilated cages and in a 12-h light-dark cycle with ad libitum access to food and water. For metastasis studies, 10^6 AGS cells were injected into tail veins of nude mice. At ~6 wk after injection, the animals were euthanized, and the lungs were isolated and weighed. The number and size of lung metastases detected by hematoxylin–eosin (H&E) staining were assessed.

Western Blotting. For Western blots, samples were separated on sodium dodecyl sulfate polyacrylamide gel electrophoresis (SDS-PAGE) gels and then transferred to polyvinylidene fluoride membranes (Millipore). Membranes were processed according to the ECL Western blotting protocol (GE Healthcare). The following antibodies were used in Western blots: anti-FLAG (Proteintech, 20543-1-AP), hnRNPM (Proteintech, 26897-1-AP), and anti-β-actin (TransGen, HC201). Antibody validation is provided on the manufacturers' websites.

Wound-Healing and Transwell Assays. For the wound-healing assay, after transfection for 48 h, cells were seeded in 6-well plates with Culture-Insert 2 Well (μ-Dish 35 mm, high ibiTreat) according to the manufacturer's instruction and then incubated in medium containing 2% fetal bovine serum (FBS). The width of the scratch was measured at 24 h using a light microscope. For the transwell assay, matrigel (BD Biosciences) was diluted with serum-free medium (1:8), mixed, and used to coat the insert chamber membrane. In total, 5×10^5 cells with 48-h transfection in serum-free medium were added to the upper chamber, and medium containing 10% FBS was added to the lower chamber. After incubation for 24 h, the remaining cells in the upper compartment were completely removed, and then the migrated cells on the membrane were stained by 0.1% crystal violet for 10 min. Finally, the number of cells that invaded into the lower chambers was counted under an inverted microscope (Olympus).

RNA Pulldown and RNA Immunoprecipitation. RNA pulldown with 5′-biotinylated antisense oligos and RNA IP were performed as previously described (60). The following antibodies were used: anti-FLAG (Sigma, F1804), anti-AGO2 (Sigma, SAB4200085), and anti-hnRNPM (OriGene, TA301557).

MS. MS was performed as previously described with minor modifications (60). In brief, specific and obvious silver-stained band was cut, cleaned, and digested in-gel with sequencing grade-modified trypsin (Promega) in the digestion buffer (100 mM NH_4HCO_3, pH 8.5). After extraction and purification, the peptide samples were analyzed by a Nano liquid chromatography electrospray ionization–MS/MS system. The mass spectrometric data were searched against the UniProt protein database with ProtTech's ProtQuest software suite.

Circularization In Vitro. The synthesis of circRNAs in vitro was carried out as previously described with minor modification (64). Briefly, a biotin-labeled circRNA precursor was synthesized with a Biotin RNA labeling kit (Epicentre). After DNase treatment, additional GTP was added to a final concentration of 2 mM along with a circularization buffer including magnesium (50 mM Tris [pH 7.5], 15 mM $MgCl_2$, and 1 mM DTT,) and then the reaction was heated at 55 °C for 20 min. To enrich for circRNA, RNase R-digested RNA was separated on 5% Urea PAGE gel. Bands corresponding to circRNA were excised from the gel and eluted overnight in elution buffer (20 mM Tris [pH 7.5], 250 mM NaOAc, 1 mM ethylene diamine tetraacetic acid, and 0.25% SDS). The eluted RNA was then purified using phenol/chloroform (pH 4.5). The circRNAs in vitro synthesized could be examined from the endogenous circRNAs due to a small stretch of added sequences (29 nt) involved in *SI Appendix*, Table S5.

Sucrose Density Gradients. Sucrose density gradients were carried out as previously described, with several modifications (65). Sucrose gradients (5 to 30%) were poured using the Biocomp gradient station model 153 (BioComp) and contained 50 mM Tris (pH 8.5), 150 mM NaCl, and 1 mM EDTA. Total AGS cell lysates were loaded in 13 mL 5 to 30% sucrose gradients and centrifuged for 4 h at 40,000 rpm in a Beckman SW41 Ti rotor. Following centrifugation, fractions (1 mL) were collected manually from the top. All fractions were further used for protein and RNA analysis.

Statistical Analysis. In all experiments, Student's *t* tests and χ^2 tests were used to calculate *P* values, as indicated in the figure legends. For Student's *t* tests, the values reported in the graphs represent averages of three independent experiments, with error bars showing SEM. After ANOVA with F-tests, the statistical significance and *P* values were evaluated with Student's *t* tests.

1. F. Bray *et al.*, Global cancer statistics 2018: GLOBOCAN estimates of incidence and mortality worldwide for 36 cancers in 185 countries. *CA Cancer J. Clin.* **68**, 394–424 (2018).
2. E. C. Smyth, M. Nilsson, H. I. Grabsch, N. C. van Grieken, F. Lordick, Gastric cancer. *Lancet* **396**, 635–648 (2020).
3. E. D. Williams, D. Gao, A. Redfern, E. W. Thompson, Controversies around epithelial-mesenchymal plasticity in cancer metastasis. *Nat. Rev. Cancer* **19**, 716–732 (2019).
4. L. S. Kristensen *et al.*, The biogenesis, biology and characterization of circular RNAs. *Nat. Rev. Genet.* **20**, 675–691 (2019).
5. W. R. Jeck *et al.*, Circular RNAs are abundant, conserved, and associated with ALU repeats. *RNA* **19**, 141–157 (2013).
6. L. Chen, C. Huang, X. Wang, G. Shan, Circular RNAs in eukaryotic cells. *Curr. Genomics* **16**, 312–318 (2015).
7. X. Liu *et al.*, Identification of mecciRNAs and their roles in the mitochondrial entry of proteins. *Sci. China Life Sci.* **63**, 1429–1449 (2020).
8. J. N. Vo *et al.*, The landscape of circular RNA in cancer. *Cell* **176**, 869–881.e13 (2019).
9. W. W. Du *et al.*, Foxo3 circular RNA retards cell cycle progression via forming ternary complexes with p21 and CDK2. *Nucleic Acids Res.* **44**, 2846–2858 (2016).
10. S. Chen *et al.*, Widespread and functional RNA circularization in localized prostate cancer. *Cell* **176**, 831–843.e22 (2019).
11. D. Hanniford *et al.*, Epigenetic silencing of CDR1as drives IGF2BP3-mediated melanoma invasion and metastasis. *Cancer Cell* **37**, 55–70.e15 (2020).
12. T. B. Hansen *et al.*, Natural RNA circles function as efficient microRNA sponges. *Nature* **495**, 384–388 (2013).
13. S. Memczak *et al.*, Circular RNAs are a large class of animal RNAs with regulatory potency. *Nature* **495**, 333–338 (2013).
14. Q. Zheng *et al.*, Circular RNA profiling reveals an abundant circHIPK3 that regulates cell growth by sponging multiple miRNAs. *Nat. Commun.* **7**, 11215 (2016).
15. L. Yang *et al.*, Engagement of circular RNA HECW2 in the nonautophagic role of ATG5 implicated in the endothelial-mesenchymal transition. *Autophagy* **14**, 404–418 (2018).
16. Z. Li *et al.*, Exon-intron circular RNAs regulate transcription in the nucleus. *Nat. Struct. Mol. Biol.* **22**, 256–264 (2015).

CELL BIOLOGY

CHEMISTRY

17. I. Legnini *et al.*, Circ-ZNF609 is a circular RNA that can be translated and functions in myogenesis. *Mol. Cell* **66**, 22–37.e9 (2017).
18. Y. Yang *et al.*, Extensive translation of circular RNAs driven by N[6]-methyladenosine. *Cell Res.* **27**, 626–641 (2017).
19. J. Chen *et al.*, Circular RNA profile identifies circPVT1 as a proliferative factor and prognostic marker in gastric cancer. *Cancer Lett.* **388**, 208–219 (2017).
20. F. Yang *et al.*, *Circ-HuR* suppresses HuR expression and gastric cancer progression by inhibiting CNBP transactivation. *Mol. Cancer* **18**, 158 (2019).
21. T. Maniatis, B. Tasic, Alternative pre-mRNA splicing and proteome expansion in metazoans. *Nature* **418**, 236–243 (2002).
22. X. D. Fu, M. Ares Jr, Context-dependent control of alternative splicing by RNA-binding proteins. *Nat. Rev. Genet.* **15**, 689–701 (2014).
23. H. Dvinge, J. Guenthoer, P. L. Porter, R. K. Bradley, RNA components of the spliceosome regulate tissue- and cancer-specific alternative splicing. *Genome Res.* **29**, 1591–1604 (2019).
24. H. Climente-González, E. Porta-Pardo, A. Godzik, E. Eyras, The functional impact of alternative splicing in cancer. *Cell Rep.* **20**, 2215–2226 (2017).
25. I. Lokody, Alternative splicing: Aberrant splicing promotes colon tumour growth. *Nat. Rev. Cancer* **14**, 382–383 (2014).
26. R. Xie *et al.*, Polypyrimidine tract binding protein 1 promotes lymphatic metastasis and proliferation of bladder cancer via alternative splicing of MEIS2 and PKM. *Cancer Lett.* **449**, 31–44 (2019).
27. Y. Xu *et al.*, Cell type-restricted activity of hnRNPM promotes breast cancer metastasis via regulating alternative splicing. *Genes Dev.* **28**, 1191–1203 (2014).
28. T. Geuens, D. Bouhy, V. Timmerman, The hnRNP family: Insights into their role in health and disease. *Hum. Genet.* **135**, 851–867 (2016).
29. F. Rashid, A. Shah, G. Shan, Long non-coding RNAs in the cytoplasm. *Genomics Proteomics Bioinformatics* **14**, 73–80 (2016).
30. J. J. Quinn, H. Y. Chang, Unique features of long non-coding RNA biogenesis and function. *Nat. Rev. Genet.* **17**, 47–62 (2016).
31. B. Yu, G. Shan, Functions of long noncoding RNAs in the nucleus. *Nucleus* **7**, 155–166 (2016).
32. T. M. Wheeler *et al.*, Targeting nuclear RNA for in vivo correction of myotonic dystrophy. *Nature* **488**, 111–115 (2012).
33. J. S. Lee, J. T. Mendell, Antisense-mediated transcript knockdown triggers premature transcription termination. *Mol. Cell* **77**, 1044–1054.e3 (2020).
34. F. Lai, S. S. Damle, K. K. Ling, F. Rigo, Directed RNase H cleavage of nascent transcripts causes transcription termination. *Mol. Cell* **77**, 1032–1043.e4 (2020).
35. Z. Song *et al.*, Antisense oligonucleotide technology can be used to investigate a circular but not linear RNA-mediated function for its encoded gene locus. *Sci. China Life Sci.* **64**, 784–794 (2020).
36. D. B. Dudekula *et al.*, CircInteractome: A web tool for exploring circular RNAs and their interacting proteins and microRNAs. *RNA Biol.* **13**, 34–42 (2016).
37. K. V. Datar, G. Dreyfuss, M. S. Swanson, The human hnRNP M proteins: Identification of a methionine/arginine-rich repeat motif in ribonucleoproteins. *Nucleic Acids Res.* **21**, 439–446 (1993).
38. J. König *et al.*, iCLIP reveals the function of hnRNP particles in splicing at individual nucleotide resolution. *Nat. Struct. Mol. Biol.* **17**, 909–915 (2010).
39. B. J. Zarnegar *et al.*, irCLIP platform for efficient characterization of protein-RNA interactions. *Nat. Methods* **13**, 489–492 (2016).
40. Y. Hosono *et al.*, Oncogenic role of THOR, a conserved cancer/testis long non-coding RNA. *Cell* **171**, 1559–1572.e20 (2017).
41. H. Ennajdaoui *et al.*, IGF2BP3 modulates the interaction of invasion-associated transcripts with RISC. *Cell Rep.* **15**, 1876–1883 (2016).
42. S. C. Huelga *et al.*, Integrative genome-wide analysis reveals cooperative regulation of alternative splicing by hnRNP proteins. *Cell Rep.* **1**, 167–178 (2012).
43. A. Damianov *et al.*, Rbfox proteins regulate splicing as part of a large multiprotein complex LASR. *Cell* **165**, 606–619 (2016).
44. K. O. West *et al.*, The splicing factor hnRNP M is a critical regulator of innate immune gene expression in macrophages. *Cell Rep.* **29**, 1594–1609.e5 (2019).
45. J. D. Ransohoff, Y. Wei, P. A. Khavari, The functions and unique features of long intergenic non-coding RNA. *Nat. Rev. Mol. Cell Biol.* **19**, 143–157 (2018).
46. L. Gao *et al.*, Circular RNAs from *BOULE* play conserved roles in protection against stress-induced fertility decline. *Sci. Adv.* **6**, eabb7426 (2020).
47. A. Rybak-Wolf *et al.*, Circular RNAs in the mammalian brain are highly abundant, conserved, and dynamically expressed. *Mol. Cell* **58**, 870–885 (2015).
48. J. S. Ho *et al.*, HNRNPM controls circRNA biogenesis and splicing fidelity to sustain cancer cell fitness. *eLife* **10**, e59654 (2021).
49. S. Gao *et al.*, TFPI2AS1, a novel lncRNA that inhibits cell proliferation and migration in lung cancer. *Cell Cycle* **16**, 2249–2258 (2017).
50. X. Wang *et al.*, Upregulated expression of long non-coding RNA, LINC00460, suppresses proliferation of colorectal cancer. *J. Cancer* **9**, 2834–2843 (2018).
51. E. S. Alshammari *et al.*, ERK3 is transcriptionally upregulated by ΔNp63α and mediates the role of ΔNp63α in suppressing cell migration in non-melanoma skin cancers. *BMC Cancer* **21**, 155 (2021).
52. N. Agrawal *et al.*, Comparative genomic analysis of esophageal adenocarcinoma and squamous cell carcinoma. *Cancer Discov.* **2**, 899–905 (2012).
53. J. P. Theurillat *et al.*, URI is an oncogene amplified in ovarian cancer cells and is required for their survival. *Cancer Cell* **19**, 317–332 (2011).
54. J. Yang *et al.*, Guidelines and definitions for research on epithelial-mesenchymal transition. *Nat. Rev. Mol. Cell Biol.* **21**, 341–352 (2020).
55. W. R. English *et al.*, Differential expression of VEGFA isoforms regulates metastasis and response to anti-VEGFA therapy in sarcoma. *Cancer Res.* **77**, 2633–2646 (2017).
56. N. Ferrara, R. S. Kerbel, Angiogenesis as a therapeutic target. *Nature* **438**, 967–974 (2005).
57. C. S. Fuchs *et al.*, Ramucirumab monotherapy for previously treated advanced gastric or gastro-oesophageal junction adenocarcinoma (REGARD): An international, randomised, multicentre, placebo-controlled, phase 3 trial. *Lancet* **383**, 31–39 (2014).
58. Cancer Genome Atlas Research Network, Comprehensive molecular characterization of gastric adenocarcinoma. *Nature* **513**, 202–209 (2014).
59. N. Romero-Barrios, M. F. Legascue, M. Benhamed, F. Ariel, M. Crespi, Splicing regulation by long noncoding RNAs. *Nucleic Acids Res.* **46**, 2169–2184 (2018).
60. S. Hu, X. Wang, G. Shan, Insertion of an Alu element in a lncRNA leads to primate-specific modulation of alternative splicing. *Nat. Struct. Mol. Biol.* **23**, 1011–1019 (2016).
61. A. J. Zimmerman *et al.*, A psychiatric disease-related circular RNA controls synaptic gene expression and cognition. *Mol. Psychiatry* **25**, 2712–2727 (2020).
62. X. Wang, G. Shan, Nonradioactive Northern blot of circRNAs. *Methods Mol. Biol.* **1724**, 135–141 (2018).
63. M. J. del Prete, R. Vernal, H. Dolznig, E. W. Müllner, J. A. Garcia-Sanz, Isolation of polysome-bound mRNA from solid tissues amenable for RT-PCR and profiling experiments. *RNA* **13**, 414–421 (2007).
64. R. A. Wesselhoeft, P. S. Kowalski, D. G. Anderson, Engineering circular RNA for potent and stable translation in eukaryotic cells. *Nat. Commun.* **9**, 2629 (2018).
65. S. Macias, R. A. Cordiner, P. Gautier, M. Plass, J. F. Cáceres, DGCR8 acts as an adaptor for the exosome complex to degrade double-stranded structured RNAs. *Mol. Cell* **60**, 873–885 (2015).